INORGANIC CHEMISTRY FRONTIERS

RESEARCH ARTICLE

View Article Online
View Journal | View Issue

Cite this: *Inorg. Chem. Front.*, 2025, **12**, 2395

Multidentate chelation *via* pyridine-based molecules for high-efficiency perovskite solar cells†

Yongxiang Zhang,[a,b] Jinfeng Zhang,[b] Aiqin Sun,[b] Zhiqian Yang,[b] Mengting Han,[b] Yang Huang,[b,c] Mei Lyu,[a,e] Yan Meng,*[d] Jun Zhu *[a] and Linhua Hu *[b]

The non-radiative recombination loss at the interface between a perovskite layer and hole transport layer is one of the main sources of energy loss in perovskite solar cells (PSCs). Non-radiative recombination caused by surface defects greatly limits further improvement of power conversion efficiency (PCE). Interfacial passivation is one of the commonly used methods to improve PCE, but traditional passivation methods often involve single-point coordination, and their passivation effect is limited. In this study, we used a multi-site binding passivation method, introducing diethyl 2,6-pyridinedicarboxylate (DIP) as a passivation layer at the interface between the perovskite and the hole transport layer. The ester and pyridinium groups can interact effectively with uncoordinated Pb^{2+}, and this multidentate chelation effect can repair various defects, improve crystallization, and promote interfacial carrier transfer. As a result, the optimized device achieves an efficiency of 23.68%. Additionally, due to the hydrophobicity of DIP, the device exhibits excellent humidity stability, maintaining 89.40% of its initial PCE after 550 hours at a relative humidity of 65 ± 5%.

Received 20th December 2024,
Accepted 22nd January 2025

DOI: 10.1039/d4qi03269a

rsc.li/frontiers-inorganic

1. Introduction

Over the past few decades, metal halide perovskites have demonstrated remarkable performance in photovoltaics.[1–5] The power conversion efficiency (PCE) of perovskite solar cells (PSCs) has rapidly increased from the initial 3.8% to 26.7%.[6] However, the PCE of PSCs is still far from the theoretical Shockley–Queisser limit.[7] Polycrystalline perovskite films prepared by the solution method are loaded with large numbers of defects in the surface and bulk phases, which lead to non-radiative recombination, affect the carrier transport, and result in a reduction of the PCE.[8–14] The passivation of these surface defects is the most direct and effective strategy to improve the PCE.[15,16] To passivate surface defects, many functional molecules are used by researchers. You *et al.* reported the use of an organic halide salt, phenethylammonium iodide (PEAI) on HC$(NH_2)_2$–CH_3NH_3 mixed perovskite films for surface defect passivation. They found that the PEAI layer forms on the perovskite surface and this results in higher-efficiency cells by reducing the defects and suppressing non-radiative recombination.[17] Furthermore, other compounds such as iodopentafluorobenzene[18] and potassium halides[19] are also used to passivate surface defects. Among many molecules, pyridine derivatives have attracted our attention; they are mostly formed by combining pyridine groups with carbonyl, carboxyl or amine groups as well as halogen groups, and have demonstrated good passivation effects on defects. At the same time, the various sites on the pyridine ring can be linked to multiple functional groups, which can passivate defects to a greater extent.[20–25] However, there has been relatively little research on the multidentate chelation passivation of perovskites using pyridine derivatives. Multidentate chelation can utilize various functional groups to passivate different defects of perovskites. By attaching specific functional groups to the target sites, a synergistic passivation effect can be achieved. The multi-site binding makes the connection between functional molecules and perovskite more stable, so as to achieve a more obvious optimization effect.

Herein, we introduce a pyridine-based molecule with a rich ester group as a passivator, diethyl 2,6-pyridinedicarboxylate (DIP), which can be anchored to the surface of a perovskite. The ester and pyridyl groups interact effectively with the Pb^{2+} defect sites, to reduce the surface recombination and mini-

[a]*School of Chemistry and Chemical Engineering Hefei University of Technology, Hefei 230009, China. E-mail: jzhu@hfut.edu.cn*
[b]*Key Laboratory of Photovoltaic and Energy Conservation Materials, CAS, Institute of Solid State Physics, Hefei Institutes of Physical Science, Chinese Academy of Sciences, Hefei, Anhui, 230031, China. E-mail: lhhu@rntek.cas.cn*
[c]*Anhui Institute of Innovation for Industrial Technology, Hefei, Anhui 230088, China*
[d]*Department of Physics, Xingtai University, Xingtai, Hebei, 054001, China. E-mail: 200221007@xttc.edu.cn*
[e]*Postdoctoral Workstation, AnHui SunWay Cable Co., Ltd, No. 18, Gaoxin Avenue, Gaogou Industrial District, Wuwei, 238339, China*

† Electronic supplementary information (ESI) available. See DOI: https://doi.org/10.1039/d4qi03269a

mize the formation of defects. Moreover, due to the excellent hydrophobic properties of the DIP molecule, its use significantly improves the stability of PSC devices. Consequently, the PSCs achieved a superior PCE value of 23.68%. These unencapsulated devices demonstrate excellent stability, and can maintain 92.96% of their initial efficiency after 1500 hours at room temperature under a nitrogen (N_2) atmosphere. Under ambient conditions with a relative humidity of 65 ± 5%, the DIP-modified device retains 89.40% of its initial PCE after 550 hours.

2. Results and discussion

The chemical structure of diethyl 2,6-pyridinedicarboxylate (DIP) is shown in Fig. 1a, which reveals that the molecule contains one pyridine group and two ester groups. Considering the presence of several strongly electronegative groups in DIP, the distribution of electrostatic potential was studied using density functional theory. As shown in Fig. 1b, variations in the electronegativity of the molecule are observed through

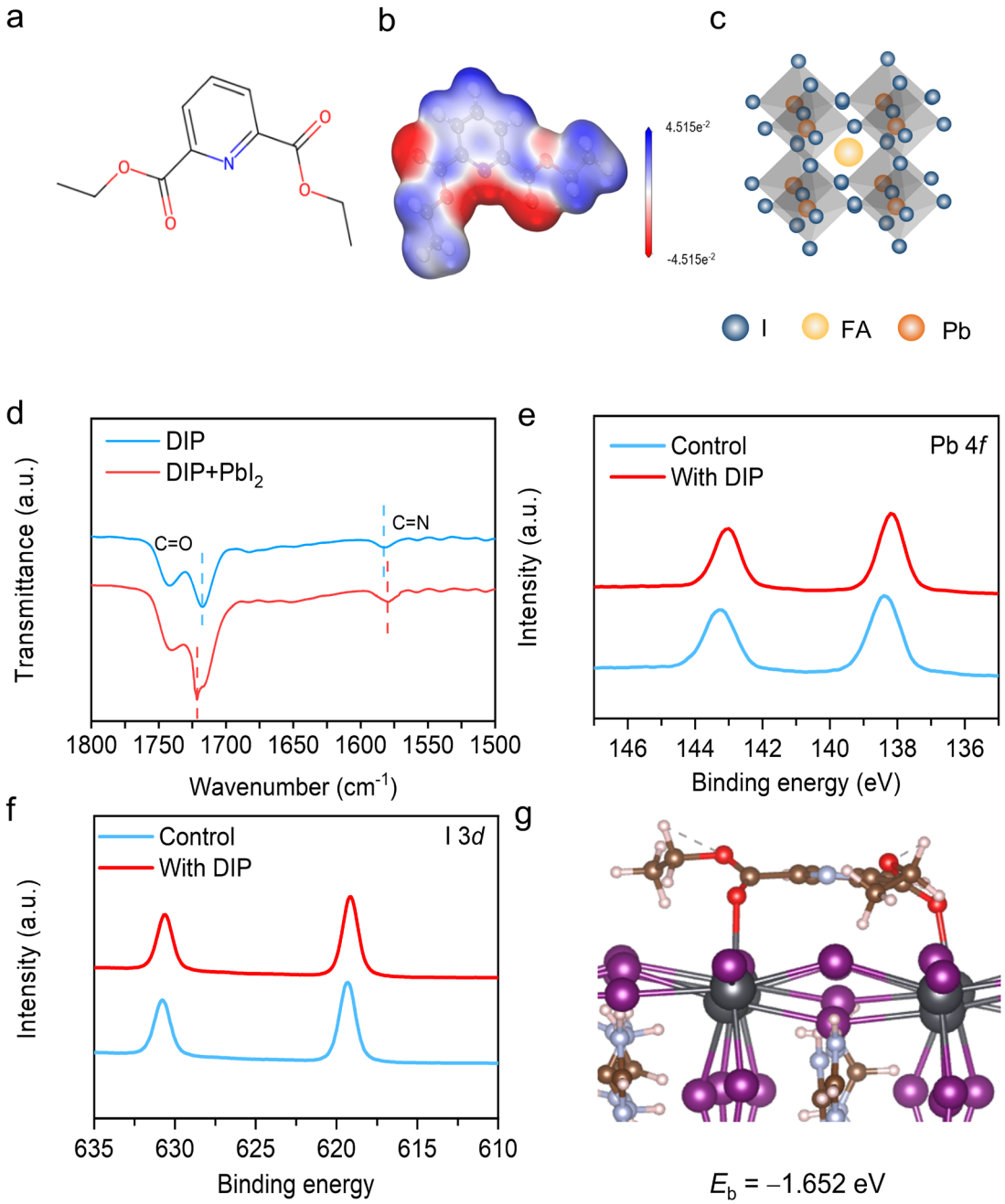

Fig. 1 (a) Chemical structure of DIP. (b) ESP surface map of the DIP molecule. (c) Structure illustration of $FAPbI_3$. (d) FTIR spectra of the solution: DIP and DIP/PbI_2 (all dissolved in DMSO). (e and f) detailed Pb 4f and I 3d XPS spectra, respectively. (g) DFT modeling of the binding energy of DIP molecules on the perovskite surface.

changes in the color of different regions of its electrostatic potential surface. The red areas on the electrostatic potential (ESP) surface of DIP highlight regions of electronegative concentration, indicating potential sites that can bind with a perovskite. We found that the red regions predominantly surround the carbonyl (C═O) and pyridyl (C═N) groups, indicating high electron density that favors their coordination with uncoordinated Pb^{2+}. Additionally, DIP undergoes efficient and reversible coordination with iodine atoms, which is expected to regulate the crystallization process and reduce trap density in the perovskite.[26] To confirm the strong interaction between DIP and PbI_2, Fourier transform infrared (FTIR) spectroscopy was used (Fig. 1d). The symmetric stretching vibrations of the C═O and C═N groups in DIP were observed at 1717.5 and 1582.8 cm^{-1}, respectively. After mixing with PbI_2, the corresponding peak positions shifted to 1721.3 and 1579.9 cm^{-1}, indicating that both the ester and pyridyl groups interact with the uncoordinated Pb^{2+} defects in the perovskite.[27–30] The interaction of DIP with perovskite was then characterized by X-ray photoelectron spectroscopy (XPS), and the survey spectra are shown in Fig. 1e and f. In the control film, the XPS characterization of Pb 4f shows two dominant peaks at 143.27 and 138.38 eV, which could be assigned to Pb $4f^{5/2}$ and Pb $4f^{7/2}$, while the Pb 4f peaks shifted toward lower binding energy (143.05 eV for Pb $4f^{5/2}$ and 138.18 eV for Pb $4f^{7/2}$) after DIP passivation. The shift of the peaks demonstrated the decrease in the positive charge of the uncoordinated Pb^{2+}, resulting from the donation of the electron pair of the N atom of the C═N group and the O atom of the C═O group to the empty 6p orbital of the uncoordinated Pb^{2+} according to the coordination bond.[31] The characteristic I $3d^{3/2}$ and I $3d^{5/2}$ peaks of the control perovskite film were located at 630.81 and 619.32 eV, respectively, and these signals shifted toward lower binding energy (630.62 eV for I $3d^{3/2}$ and 619.17 eV for I $3d^{5/2}$) after DIP passivation. These shifts of the peaks are similar to the abovementioned shift of the Pb 4f peaks. According to the detections in the FTIR and XPS spectra, we verified strong interaction between the DIP and the perovskite. The C═O and C═N groups could interact with the uncoordinated Pb^{2+} defects and I^- defects in the perovskite to repair the uncoordinated ionic defects.[32] We then calculated the binding energy of the perovskite in different binding states (Fig. S1†). The calculation results revealed that the binding energy of the bidentate chelation configuration is much higher than the binding energy of the monodentate model and, in particular, the binding energy value of the two ester groups chelated at the same time is the largest (Fig. 1g), which is −1.652 eV.

Furthermore, in order to investigate the grain boundary and defects at the surface of the perovskite film, Kelvin probe force microscopy (KPFM) was conducted to analyze the surface potential of different perovskite films (Fig. 2a). During the linear scan, the tip of the probe travels through the grain interior and grain boundary. By observing the change in the surface potential of the perovskite (Fig. 2b), we can establish the defect state of the grain boundary and film surface. The deep-level defects have much lower formation energies and are more likely to form at grain boundaries and/or the surface of perovskite films, thus leading to significant changes in the surface potentials.[33] According to the KPFM results, the surface potential distribution over the DIP-modified perovskite film was more homogeneous and had less variation, which proved that the defect states at grain boundaries and the film surface were obviously reduced. The more homogeneous surface potential suggests that it would be more beneficial for carrier transfer to take place in the transport layer.[34,35] Moreover, the DIP treatment can also reduce film roughness from ~33.0 nm (control) to ~28.4 nm (target), flattening the height differences between the grain surface and grain boundary (GB) (Fig. S2†). The detailed surface morphology of a perovskite film with or without DIP modification was observed by scanning electron microscopy (SEM). As shown in Fig. 2c, the top-view SEM image of the perovskite film without DIP shows some holes and small grains. In contrast, the DIP-modified perovskite film shows larger grain sizes, and the holes have disappeared. This implied that the interaction between DIP and the perovskite promoted larger sized perovskite grains during the formation of perovskite crystals.[36,37] The cross-sectional image shows the same results in Fig. S3.† X-ray diffraction (XRD) measurements were performed to analyze the crystallinity of the perovskite films before and after DIP modification (Fig. 2d). It can be found that the control perovskite film showed a strong PbI_2 signal at 12.8°, while the DIP-modified perovskite film exhibited a weaker PbI_2 signal and stronger peak corresponding to (001), indicating that the perovskite with DIP modification acquires much stronger crystallinity. The ratio of α-phase $FAPbI_3$ peak intensity to PbI_2 peak intensity is 4.95 for the control device and 8.80 for the DIP-modified device (Fig. S4†). The performance of the perovskite films was evaluated by steady-state photoluminescence (PL) measurements (Fig. 2e). Compared to the pristine perovskite, the stronger PL intensity of the DIP-modified perovskite suggests that non-radiative recombination is inhibited. The PL mappings show that the target film exhibits enhanced luminescence intensity compared to the control. It is also demonstrated that DIP is uniformly distributed on the surface of the film, contributing to the enhancement of its PL intensity (Fig. S5†). Time-resolved photoluminescence (TRPL) decay measurements were conducted to probe the fluorescence lifetime of the perovskite film (Fig. 2f). The fitted decay times of the corresponding perovskite films are summarized in Table S1.† The TRPL profiles of the control and DIP-modified perovskite films were fitted with a biexponential function. We observed a longer carrier lifetime (τ_1 = 172.15 ns; τ_2 = 1004.53 ns) in the DIP-modified perovskite film compared to that in the perovskite film without DIP modification (τ_1 = 42.89 ns; τ_2 = 232.07 ns). The calculated average carrier lifetime of the DIP-modified samples is 739.83 ns, much longer than that of the control samples (143.82 ns), indicating that carrier non-radiative recombination loss is significantly suppressed in DIP-modified perovskite films.[38]

To evaluate the passivation effect of DIP, Fig. 3a shows the formation energy of iodine vacancy (V_I), anti-site lead–iodine

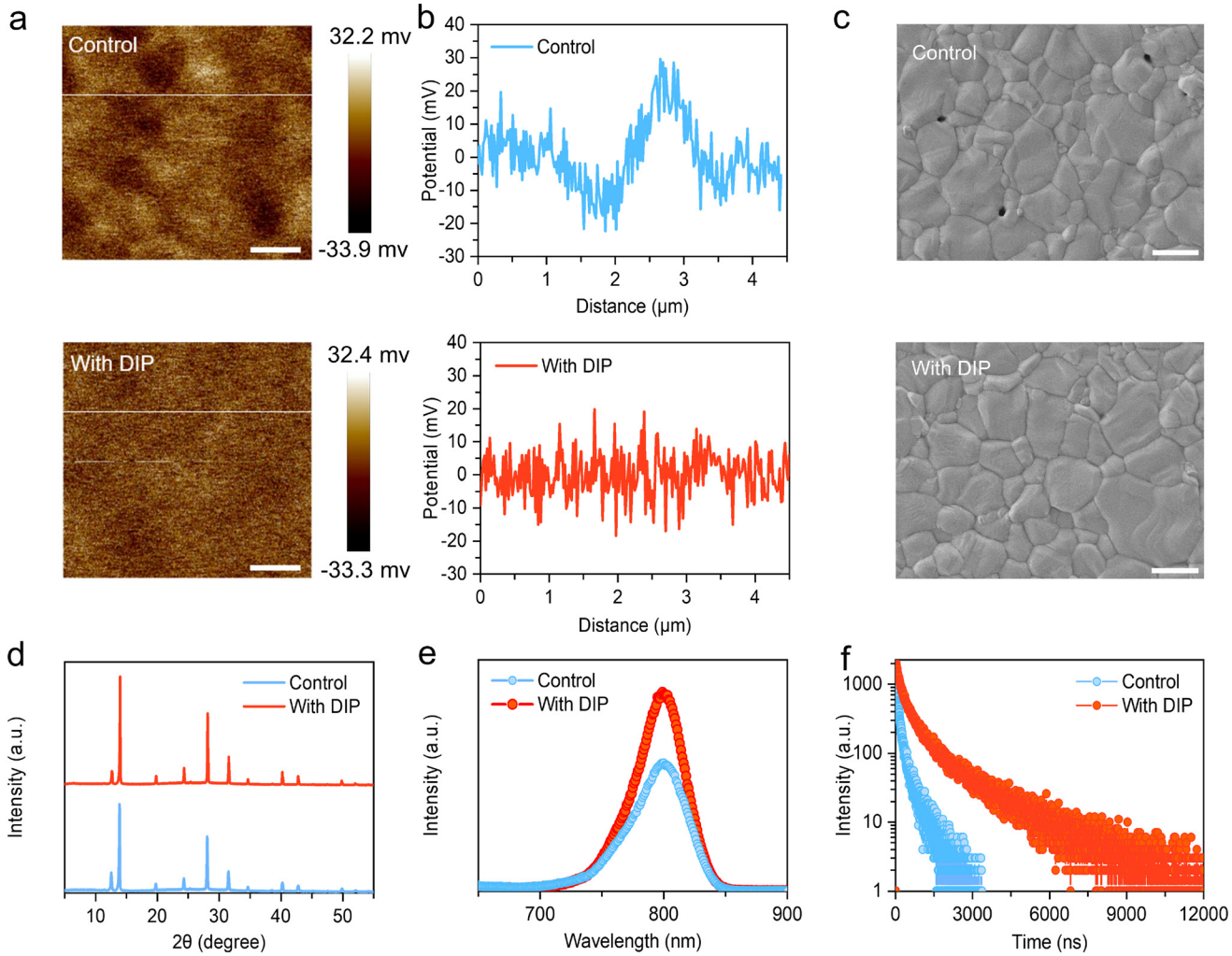

Fig. 2 (a) The KPFM images of the control and DIP-modified perovskite films (scale bar, 1 μm). (b) The surface potential line profiles of the control and DIP-modified perovskite films. (c) SEM images of perovskite films without and with DIP modification coated on glass (scale bar, 1 μm). (d) XRD patterns of the perovskite film with and without DIP modification. (e) PL spectra of the perovskite films with and without DIP modification. (f) TRPL spectra of the perovskite films with and without DIP modification.

(Pb_I), anti-site iodine–lead (I_{Pb}), FA vacancy (V_{FA}) and Pb vacancy (V_{Pb}) defects on the perovskite surface. Clearly, DIP treatment leads to greatly increased formation energy, which means the corresponding defects are harder to form.[39] Furthermore, to reveal the effect of DIP on the properties of perovskite films, ultraviolet photo-electron spectroscopy (UPS) was used to study the surface energetics of perovskite films (Fig. S6†). According to the results indicated in Fig. 3b, the conduction band minimum (CBM) and valence band maximum (VBM) of perovskite films without and with DIP modification could be obtained by UPS and ultraviolet–visible (UV–vis) absorption spectroscopy (Fig. S7†). The CBM was adjusted from −3.91 eV to −3.89 eV upon DIP modification. The upward-bending VBM of DIP-processed films more favorably aligns with the HOMO energy levels of spiro-OMeTAD, facilitating hole extraction and alleviating carrier accumulation.[40] Subsequently, hole-only devices with FTO/PEDOT:PSS/PVK/spiro-OMeTAD/Au structures were prepared to quantitatively assess the trap-state density and hole mobility using the space charge limited current (SCLC) strategy (Fig. 3c). The trap-state density (N_t) of the electron transport layer (ETL) can be estimated through the following equation:

$$V_{TFL} = eN_tL^2/2\varepsilon\varepsilon_0$$

where e and L are the elementary charge and the thickness of the films, and ε and ε_0 are the dielectric constant and the vacuum permittivity, respectively.[41–43] The V_{TFL} values of the control and target are 0.439 V and 0.343 V, respectively. This suggests that DIP can effectively reduce the trap states, consequently suppressing non-radiative recombination.[44] As evidenced by the dark J–V curves shown in Fig. S8,† the dark saturation current of the DIP-modified PSCs is smaller than that of the control PSCs, indicating the decreased non-radiative

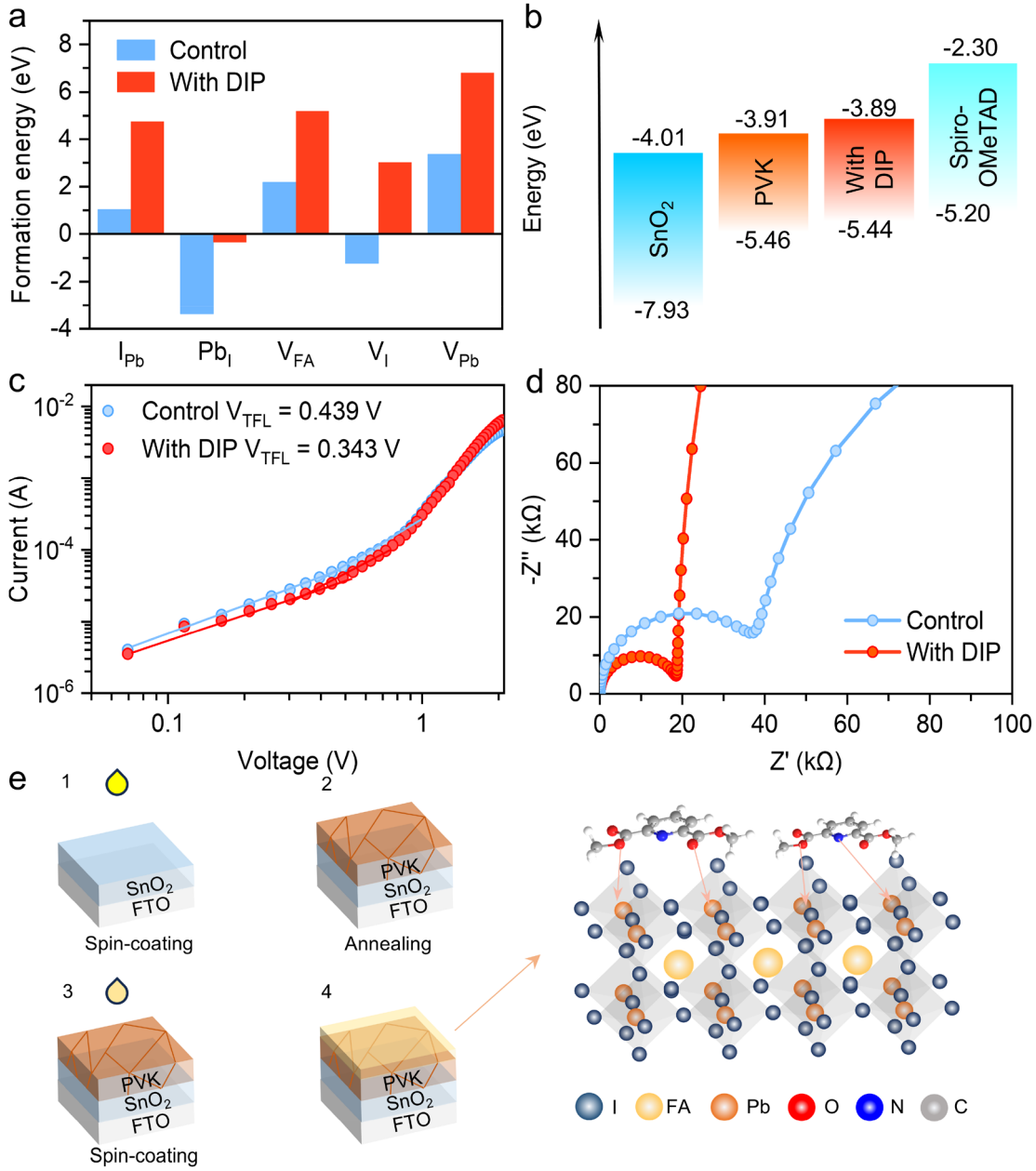

Fig. 3 (a) Formation energy values of perovskite surface V_I, V_{Pb}, V_{FA}, Pb_I and I_{Pb} defects with and without DIP modification. (b) Schematic diagram of the energy level structure. (c) The space charge limited current *versus* voltage of hole-only devices with and without DIP modification. (d) Nyquist plots of PSCs with and without DIP modification. (e) Illustration of the roles of the DIP treatment in the PSCs.

recombination after DIP passivation at the interface.[45] To systematically investigate the reasons for the improved device performance, electrochemical impedance spectroscopy (EIS) was performed in the dark to study interfacial charge transfer and recombination (Fig. 3d). The semicircle in the high frequency region and the semicircle in the low frequency region determine the charge transfer resistance (R_{ct}) and the recombination resistance (R_{rec}), respectively. It can be seen that the DIP-modified device has larger R_{rec} and smaller R_{ct} values compared to those of the control device, indicating that DIP can effectively inhibit charge recombination at the interface.[45,46] The Mott–Schottky curve (Fig. S9†) reveals an increased built-in potential (V_{bi}) for the DIP-modified device, which shows a higher V_{bi} response than the control device. The increased V_{bi} can enhance the driving force and carrier injection, which is also the reason for the increase in V_{oc}.

Based on the above results, a schematic diagram illustrating the passivation mechanism of DIP was proposed, as shown in Fig. 3e. The two ester groups and one pyridine group of DIP can readily interact with Pb^{2+} defect sites, anchoring to the surface of the perovskite, which can reduce surface recombination, and reduce the formation of defects. The synergistic

impact of these beneficial effects can significantly reduce defects in perovskite films, ultimately facilitating the generation of pinhole-free, large-grained and highly crystalline perovskite films, improving the device efficiency.

Then, the effects of DIP on the device performance of PSCs were systematically studied. PSC devices with and without DIP addition were fabricated to examine their photovoltaic performance. As shown in Fig. 4a, a standard device structure of FTO/SnO_2/PVK/spiro-OMeTAD/Au was used. The optimal photoelectric performance parameters of the control and the DIP-modified devices under AM 1.5G illumination at 100 mW cm^{-2} are shown in Table S2 and Fig. S10.† The *J–V* curves of the best PSCs are shown in Fig. 4b, Whereas the control device gives a PCE of 22.15%, the DIP-modified device delivers a significantly improved PCE of up to 23.68% with an increased J_{sc} value of 25.83 mA cm^{-2}, a V_{oc} of 1.13 V, and an FF of 81.05%. Fig. 4c shows the monochromatic incident photon-to-electron conversion efficiency (IPCE) spectra for these PSCs. The integrated current densities are 24.80 and 25.10 mA cm^{-2} for the control and DIP-treated PSCs, respectively. The remarkable PCE enhancement is mainly dominated by the significant increase in V_{oc} and FF, which is attributed to the more efficient carrier extraction and passivation of defects induced by DIP.

To study the effect of DIP on the perovskite stability, we carried out XRD measurements on perovskite films that had been aged for 30 days under relative humidity of 65 ± 5%. As shown in Fig. 4d and g, the initial perovskite phase of the control sample was largely transformed into either PbI_2 (at 12.7°) or a non-perovskite δ-phase (at 11.8°). However, for the DIP-modified perovskite film, the initial perovskite phase shows only partial decomposition or phase change after moisture erosion, affirming its improved stability. The ratio of α-phase peak intensity to PbI_2 peak intensity is shown in

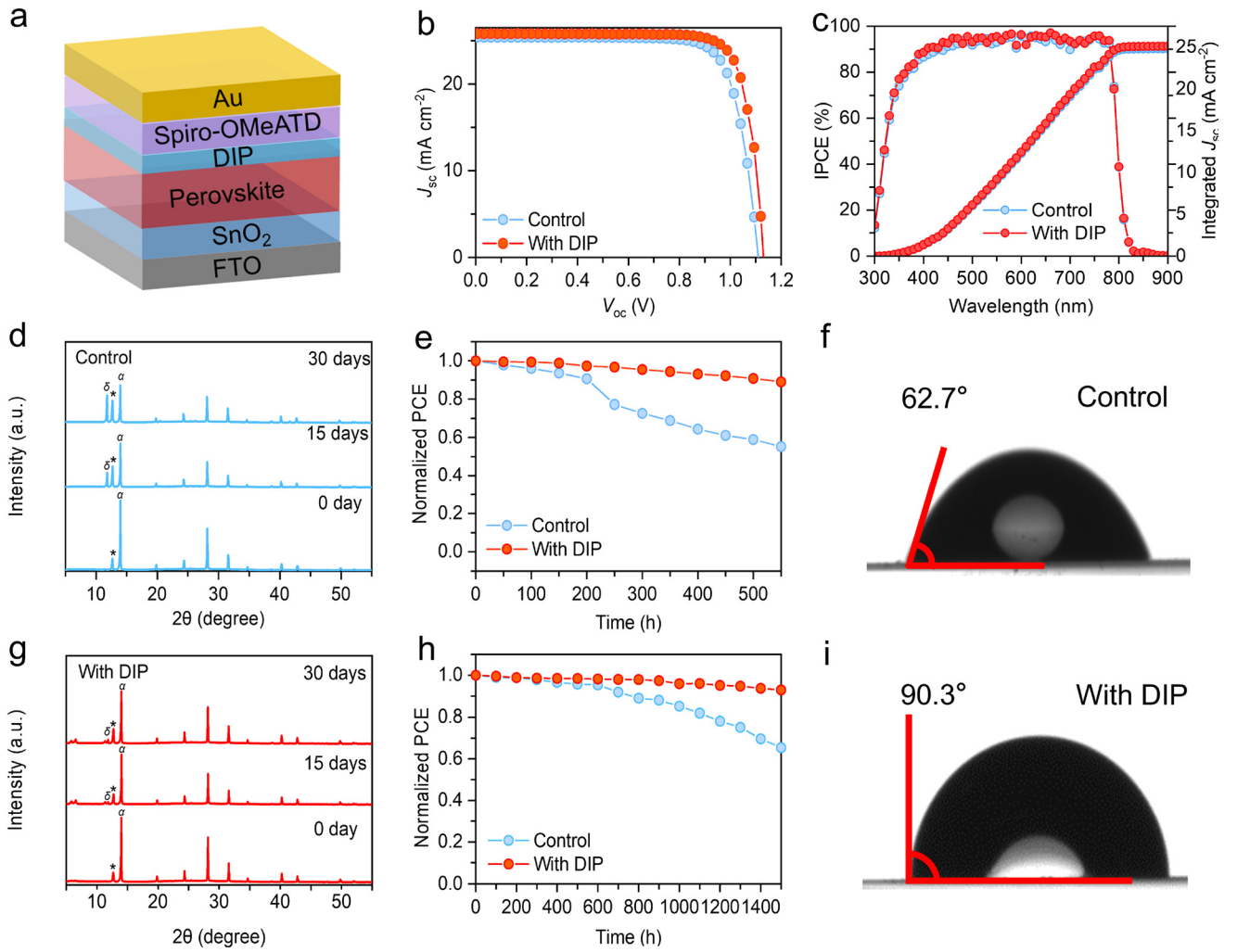

Fig. 4 (a) Schematic of the complete architecture of a PSC device. (b) *J–V* curve of the best performing device with or without DIP modification. (c) The IPCE spectra and integrated J_{sc} values. (d and g) XRD patterns of control and DIP-treated perovskite films after 30 days aged at relative humidity of 65 ± 5%. (e) Normalized PCE of the unencapsulated device with and without DIP modification at the relative humidity of 65 ± 5%. (h) Normalized PCE of the unencapsulated device with and without DIP modification at 25 ± 5 °C under dark ambient conditions in an N_2 glovebox. (f and i) Water contact angles of control and target perovskite films.

Fig. S11.† We measured the water contact angle of the control and target perovskite films (Fig. 4f and i). The control film shows a water contact angle of 62.7°, and the DIP-modified perovskite film shows a water contact angle of 90.3°, indicating that DIP can confer improved stability in a humid environment. Then, the PCEs of the devices were examined under different storage conditions. Under ambient conditions with a relative humidity of 65 ± 5% (Fig. 4e), the control device retained just 55.29% of its initial PCE value after 550 h. In contrast, the DIP-modified device could maintain 89.40% of its initial PCE, which can be attributed to the enhanced hydrophobic properties after DIP treatment. For the aged stability test at 25 ± 5 °C under N_2 (Fig. 4h), after 1500 h, the control device retained just 65.38% of its initial PCE, while the DIP-modified device could maintain 92.96% of its initial PCE. These results fully demonstrate the excellent stability of DIP-modified PSCs, confirming the improved stability induced by DIP treatment. The introduction of DIP will help enhance the comprehensive stability of PSCs, which is critical for the further application of PSC technology.

3. Conclusion

In summary, a multidentate coordination strategy using diethyl 2,6-pyridinedicarboxylate (DIP) as an additive was employed to regulate crystal growth and inhibit defects in perovskite solar cells (PSCs). Systematic theoretical analyses indicate strong intermolecular interactions between $FAPbI_3$ with defects and DIP *via* the multidentate coordination effect. DIP can be anchored to the perovskite surface, with its ester and pyridine groups interacting effectively with Pb^{2+} defect sites, which reduces surface recombination and minimizes defect formation. As a result, higher crystallinity was achieved in the subsequent formation of perovskite films. Ultimately, DIP-modified devices exhibited prolonged carrier lifetimes and enhanced built-in voltage, leading to significantly improved power conversion efficiency (PCE) of 23.68%. This work highlights the passivation effect of pyridinyl derivatives in PSCs and demonstrates that the synergistic passivation by a multidentate molecule provides valuable insights for improving PSC performance.

Author contributions

Yongxiang Zheng: investigation, data curation, and writing – original draft. Jinfeng Zhang: investigation and formal analysis. Aiqin Sun: investigation and formal analysis. Zhiqian Yang: investigation and formal analysis. Mengting Han: investigation. Yan Meng: formal analysis. Yan Meng and Mei Lyu: formal analysis. Yang Huang: conceptualization, methodology, and writing – review & editing. Jun Zhu: funding acquisition, methodology, and formal analysis. Linhua Hu: funding acquisition, supervision, and project administration.

Data availability

The data supporting this article have been included as part of the ESI.†

Conflicts of interest

There are no conflicts to declare.

Acknowledgements

This work was supported by the National Key R&D Program of China (2022YFB4200500), the Key Research and Development Plan Project of Anhui Province (2022h11020014), the National Natural Science Foundation of China (52302237) and the Collaborative Innovation Program of Hefei Science Center, CAS (2022HSC-CIP006), the CASHIPS Director's Fund (YZJJ201902 and YZJJZX202018), the Anhui Provincial Natural Science Foundation (2408085MB029), the Anhui Postdoctoral Scientific Research Program Foundation (2024B811) and the Natural Science Foundation of Hebei Province of China (B2024402018). Numerical computations were performed at the Hefei Advanced Computing Center.

References

1 J. Liu, T. Ye, D. Yu, S. (Frank) Liu and D. Yang, Recoverable Flexible Perovskite Solar Cells for Next–Generation Portable Power Sources, *Angew. Chem.*, 2023, **135**, e202307225.
2 M. Jung, S.-G. Ji, G. Kim and S. I. Seok, Perovskite Precursor Solution Chemistry: From Fundamentals to Photovoltaic Applications, *Chem. Soc. Rev.*, 2019, **48**, 2011–2038.
3 Q. Fu, X. Tang, B. Huang, T. Hu, L. Tan, L. Chen and Y. Chen, Recent Progress on the Long–Term Stability of Perovskite Solar Cells, *Adv. Sci.*, 2018, **5**, 1700387.
4 J. Y. Kim, J.-W. Lee, H. S. Jung, H. Shin and N.-G. Park, High-Efficiency Perovskite Solar Cells, *Chem. Rev.*, 2020, **120**, 7867–7918.
5 Z. Lun, L. Mei and Z. Jun, Research Progress of $Cs_2AgBiBr_6$ Perovskite Solar Cell, *J. Inorg. Mater.*, 2023, **38**(9), 1045–1054.
6 National Renewable Energy Laboratory Best Research-Cell Efficiencies Chart. **https://www.nrel.gov/pv/cell-efficiency.html** (accessed: December 2024).
7 L. Zhang, L. Mei, K. Wang, Y. Lv, S. Zhang, Y. Lian, X. Liu, Z. Ma, G. Xiao, Q. Liu, S. Zhai, S. Zhang, G. Liu, L. Yuan, B. Guo, Z. Chen, K. Wei, A. Liu, S. Yue, G. Niu, X. Pan, J. Sun, Y. Hua, W.-Q. Wu, D. Di, B. Zhao, J. Tian, Z. Wang, Y. Yang, L. Chu, M. Yuan, H. Zeng, H.-L. Yip, K. Yan, W. Xu, L. Zhu, W. Zhang, G. Xing, F. Gao and L. Ding, Advances in the Application of Perovskite Materials, *Nano-Micro Lett.*, 2023, **15**, 177.

8 X. Zheng, B. Chen, J. Dai, Y. Fang, Y. Bai, Y. Lin, H. Wei, X. C. Zeng and J. Huang, Defect Passivation in Hybrid Perovskite Solar Cells Using Quaternary Ammonium Halide Anions and Cations, *Nat. Energy*, 2017, **2**, 17102.
9 G. A. H. Wetzelaer, M. Scheepers, A. M. Sempere, C. Momblona, J. Ávila and H. J. Bolink, Trap–Assisted Non–Radiative Recombination in Organic–Inorganic Perovskite Solar Cells, *Adv. Mater.*, 2015, **27**, 1837–1841.
10 Q. Wang, Q. Dong, T. Li, A. Gruverman and J. Huang, Thin Insulating Tunneling Contacts for Efficient and Water–Resistant Perovskite Solar Cells, *Adv. Mater.*, 2016, **28**, 6734–6739.
11 N.-G. Park, Methodologies for High Efficiency Perovskite Solar Cells, *Nano Converg.*, 2016, **3**, 15.
12 S. G. Motti, D. Meggiolaro, A. J. Barker, E. Mosconi, C. A. R. Perini, J. M. Ball, M. Gandini, M. Kim, F. De Angelis and A. Petrozza, Controlling Competing Photochemical Reactions Stabilizes Perovskite Solar Cells, *Nat. Photonics*, 2019, **13**, 532–539.
13 H. Min, D. Y. Lee, J. Kim, G. Kim, K. S. Lee, J. Kim, M. J. Paik, Y. K. Kim, K. S. Kim, M. G. Kim, T. J. Shin and S. Il Seok, Perovskite Solar Cells with Atomically Coherent Interlayers on SnO_2, Electrodes, *Nature*, 2021, **598**, 444–450.
14 J. S. Manser, M. I. Saidaminov, J. A. Christians, O. M. Bakr and P. V. Kamat, Making and Breaking of Lead Halide Perovskites, *Acc. Chem. Res.*, 2016, **49**, 330–338.
15 Y. Fu, Y. Li, G. Xing and D. Cao, Surface Passivation of Perovskite with Organic Hole Transport Materials for Highly Efficient and Stable Perovskite Solar Cells, *Mater. Today Adv.*, 2022, **16**, 100300.
16 Y. Chen and H. Zhou, Defects Chemistry in High-Efficiency and Stable Perovskite Solar Cells, *J. Appl. Phys.*, 2020, **128**, 060903.
17 Q. Jiang, Y. Zhao, X. Zhang, X. Yang, Y. Chen, Z. Chu, Q. Ye, X. Li, Z. Yin and J. You, Surface Passivation of Perovskite Film for Efficient Solar Cells, *Nat. Photonics*, 2019, **13**, 460–466.
18 A. Abate, M. Saliba, D. J. Hollman, S. D. Stranks, K. Wojciechowski, R. Avolio, G. Grancini, A. Petrozza and H. J. Snaith, Supramolecular Halogen Bond Passivation of Organic–Inorganic Halide Perovskite Solar Cells, *Nano Lett.*, 2014, **14**, 3247–3254.
19 M. Abdi-Jalebi, Z. Andaji-Garmaroudi, S. Cacovich, C. Stavrakas, B. Philippe, J. M. Richter, M. Alsari, E. P. Booker, E. M. Hutter, A. J. Pearson, S. Lilliu, T. J. Savenije, H. Rensmo, G. Divitini, C. Ducati, R. H. Friend and S. D. Stranks, Author Correction: Maximizing and Stabilizing Luminescence from Halide Perovskites with Potassium Passivation, *Nature*, 2018, **555**, 497–501.
20 M. Hou, Y. Wang, X. Yang, M. Han, H. Ren, Y. Li, Q. Huang, Y. Ding, Y. Zhao, X. Zhang and G. Hou, Aryl Quaternary Ammonium Modulation for Perovskite Solar Cells with Improved Efficiency and Stability, *Nano Energy*, 2022, **94**, 106922.
21 J. Park, J. Kim, H.-S. Yun, M. J. Paik, E. Noh, H. J. Mun, M. G. Kim, T. J. Shin and S. I. Seok, Controlled Growth of Perovskite Layers with Volatile Alkylammonium Chlorides, *Nature*, 2023, **616**, 724–730.
22 R. Zhao, T. Wu, R. Zhuang, Y. Hua and Y. Wang, Unravel the Charge–Carrier Dynamics in Simple Dimethyl Oxalate–Treated Perovskite Solar Cells with Efficiency Exceeding 22%, *Energy Environ. Mater.*, 2023, **6**, e12417.
23 J. Peng, J. I. Khan, W. Liu, E. Ugur, T. Duong, Y. Wu, H. Shen, K. Wang, H. Dang, E. Aydin, X. Yang, Y. Wan, K. J. Weber, K. R. Catchpole, F. Laquai, S. De Wolf and T. P. White, A Universal Double–Side Passivation for High Open-Circuit Voltage in Perovskite Solar Cells: Role of Carbonyl Groups in Poly(Methyl Methacrylate), *Adv. Energy Mater.*, 2018, **8**, 1801208.
24 L. Yang, H. Zhou, Y. Duan, M. Wu, K. He, Y. Li, D. Xu, H. Zou, S. Yang, Z. Fang, S. Liu and Z. Liu, 25.24%-Efficiency $FACsPbI_3$ Perovskite Solar Cells Enabled by Intermolecular Esterification Reaction of DL–Carnitine Hydrochloride, *Adv. Mater.*, 2023, **35**, 2211545.
25 Y. Xu, S. Xiong, S. Jiang, J. Yang, D. Li, H. Wu, X. You, Y. Zhang, Z. Ma, J. Xu, J. Tang, Y. Yao, Z. Sun and Q. Bao, Synchronous Modulation of Defects and Buried Interfaces for Highly Efficient Inverted Perovskite Solar Cells, *Adv. Energy Mater.*, 2023, **13**, 2203505.
26 C.-H. Li, C. Wang, C. Keplinger, J.-L. Zuo, L. Jin, Y. Sun, P. Zheng, Y. Cao, F. Lissel, C. Linder, X.-Z. You and Z. Bao, A Highly Stretchable Autonomous Self-Healing Elastomer, *Nat. Chem.*, 2016, **8**, 618–624.
27 Y. Li, D. Fan, F. Xu, C. Shan, J. Yu, W. Li, D. Luo, Z. Sun, H. Fan, M. Zhao, X. Li, K. Cui, R. Chen, G. Li and A. K. K. Kyaw, 1 + 1 > 2: Dual Strategies of Quinolinic Acid Passivation and DMF Solvent Annealing for High-Performance Inverted Perovskite Solar Cell, *Chem. Eng. J.*, 2022, **435**, 135107.
28 Y.-J. Kang, S.-N. Kwon, S.-P. Cho, Y.-H. Seo, M.-J. Choi, S.-S. Kim and S.-I. Na, Antisolvent Additive Engineering Containing Dual-Function Additive for Triple-Cation p–i–n Perovskite Solar Cells with over 20% PCE, *ACS Energy Lett.*, 2020, **5**, 2535–2545.
29 Y. Wang, Z. Zhang, Y. Lan, Q. Song, M. Li and Y. Song, Tautomeric Molecule Acts as a "Sunscreen" for Metal Halide Perovskite Solar Cells, *Angew. Chem., Int. Ed.*, 2021, **60**, 8673–8677.
30 Z. Zhang, Y. Gao, Z. Li, L. Qiao, Q. Xiong, L. Deng, Z. Zhang, K. Müllen and P. Gao, Marked Passivation Effect of Naphthalene-1,8-Dicarboximides in High–Performance Perovskite Solar Cells, *Adv. Mater.*, 2021, **33**, 2008405.
31 Z. Wu, M. Jiang, Z. Liu, A. Jamshaid, L. K. Ono and Y. Qi, Highly Efficient Perovskite Solar Cells Enabled by Multiple Ligand Passivation, *Adv. Energy Mater.*, 2020, **10**, 1903696.
32 Y. Zhang, R. Yu, M. Li, Z. He, Y. Dong, Z. Xu, R. Wang, Z. Ma and Z. Tan, Amphoteric Ion Bridged Buried Interface for Efficient and Stable Inverted Perovskite Solar Cells, *Adv. Mater.*, 2024, **36**, 2310203.
33 C. Li, Z. Song, D. Zhao, C. Xiao, B. Subedi, N. Shrestha, M. M. Junda, C. Wang, C. Jiang, M. Al-Jassim, R. J. Ellingson, N. J. Podraza, K. Zhu and Y. Yan, Reducing

Saturation–Current Density to Realize High–Efficiency Low–Bandgap Mixed Tin–Lead Halide Perovskite Solar Cells, *Adv. Energy Mater.*, 2019, **9**, 1803135.

34 C. Zhang, A. Baktash, J. Zhong, W. Chen, Y. Bai, M. Hao, P. Chen, D. He, S. Ding, J. A. Steele, T. Lin, M. Lyu, X. Wen, W. Wu and L. Wang, Dual Metal–Assisted Defect Engineering towards High–Performance Perovskite Solar Cells, *Adv. Funct. Mater.*, 2022, **32**, 2208077.

35 Q. Zhang, F. Cao, Y. Wang, A. Tong, S. Wang, P. Chen, Z. Zhao, Y. Wang, W. Sun, W. Pan, Y. Li and J. Wu, Synergistic effect of ionic liquid-doped spiro OMeTAD: simultaneous management of energy level alignment and interfacial traps in perovskite solar cells, *Inorg. Chem. Front.*, 2024, **11**, 6627–6637.

36 X. Yang, D. Luo, Y. Xiang, L. Zhao, M. Anaya, Y. Shen, J. Wu, W. Yang, Y. Chiang, Y. Tu, R. Su, Q. Hu, H. Yu, G. Shao, W. Huang, T. P. Russell, Q. Gong, S. D. Stranks, W. Zhang and R. Zhu, Buried Interfaces in Halide Perovskite Photovoltaics, *Adv. Mater.*, 2021, **33**, 2006435.

37 C. Gao, S. Jia, X. Yin, Z. Li, G. Yang, J. Chen, Z. Li and X. An, Enhancing Open-Circuit Voltage in $FAPbI_3$ Perovskite Solar Cells via Self-Formation of Coherent Buried Interface $FAPbI_xCl_{3-x}$, *Chem. Commun.*, 2025, DOI: **10.1039/D4CC06599A**.

38 R. Sun, Q. Tian, M. Li, H. Wang, J. Chang, W. Xu, Z. Li, Y. Pan, F. Wang and T. Qin, Over 24% Efficient Poly (Vinylidene Fluoride) (PVDF)–Coordinated Perovskite Solar Cells with a Photovoltage up to 1.22 V, *Adv. Funct. Mater.*, 2023, **33**, 2210071.

39 B. Yang, B. Cai, T. Zhou, X. Zheng and W.-H. Zhang, Facile and Sustainable Interface Modulation via a Self-Assembly Phosphonate Molecule for Efficient and Stable Perovskite Photovoltaics, *Chem. Eng. J.*, 2024, **488**, 150861.

40 L. Liu, Y. Yang, M. Du, Y. Cao, X. Ren, L. Zhang, H. Wang, S. Zhao, K. Wang and S. (Frank) Liu, Self–Assembled Amphiphilic Monolayer for Efficient and Stable Wide–Bandgap Perovskite Solar Cells, *Adv. Energy Mater.*, 2023, **13**, 2202802.

41 V. M. Le Corre, E. A. Duijnstee, O. El Tambouli, J. M. Ball, H. J. Snaith, J. Lim and L. J. A. Koster, Revealing Charge Carrier Mobility and Defect Densities in Metal Halide Perovskites via Space-Charge-Limited Current Measurements, *ACS Energy Lett.*, 2021, **6**, 1087–1094.

42 L. Gong, J. Yang, W. Sheng, Y. Zhong, Y. Su, L. Tan and Y. Chen, Dual-Resistance of Ion Migration and Moisture Erosion via Hydrolytic Crosslinking of Siloxane Functionalized Poly(Ionic Liquids) for Efficient and Stable Perovskite Solar Cells, *CCS Chem.*, 2023, **5**, 1202–1214.

43 X. Han, H. Yao, M. Lyu, H. Lu and J. Zhu, Application of Single-molecule Liquid Crystal Additives in $CH(NH_2)_2PbI_3$ Perovskite Solar Cells, *J. Inorg. Mater.*, 2023, **38**(9), 1098–1102.

44 Z. Song, W. Xu, Y. Wu, S. Liu, W. Bi, X. Chen and H. Song, Incorporating of Lanthanides Ions into Perovskite Film for Efficient and Stable Perovskite Solar Cells, *Small*, 2020, **16**, 2001770.

45 Q. Tan, Z. Li, G. Luo, X. Zhang, B. Che, G. Chen, H. Gao, D. He, G. Ma, J. Wang, J. Xiu, H. Yi, T. Chen and Z. He, Inverted Perovskite Solar Cells Using Dimethylacridine-Based Dopants, *Nature*, 2023, **620**, 545–551.

46 X. Chen, W. Xu, Z. Shi, G. Pan, J. Zhu, J. Hu, X. Li, C. Shan and H. Song, Europium Ions Doped WO_x Nanorods for Dual Interfacial Modification Facilitating High Efficiency and Stability of Perovskite Solar Cells, *Nano Energy*, 2021, **80**, 105564.